real-time FTIR as 1-propanol was added to a dilute [Bu$_4$N][O$_2$CCN]/IL solution. This peak rapidly diminished during the addition, while concomitantly a peak corresponding to bicarbonate appeared at 1652 cm^{-1} (39). Over the course of only 2 min, v$_{as}$CO$_2$ for cyanoformate disappeared completely, while the bicarbonate peak reached a steady absorbance. All of the observed experimental results are entirely consistent with the computationally based proposal of a stepwise process for the decomposition and hydrolysis of the cyanoformate anion.

The stability of cyanoformate, a simple anion of CN$^-$ coordinated to CO$_2$, has been shown to be dependent on the dielectric constant of its local environment. We propose that this property allows it to shuttle toxic CN$^-$ away from the low-dielectric active site of the enzyme ACC oxidase before its decomposition in higher dielectric media. In broader terms, the ability to manipulate solution stability of otherwise unstable or transient species, through changes to the dielectric constant, should find other important applications.

References and Notes

1. D. Adams, S. F. Yang, *Trends Biochem. Sci.* **6**, 161–164 (1981).
2. G. D. Peiser *et al.*, *Proc. Natl. Acad. Sci. U.S.A.* **81**, 3059–3063 (1984).
3. H. Qiao *et al.*, *Science* **338**, 390–393 (2012).
4. S. P. Burg, E. A. Burg, *Science* **148**, 1190–1196 (1965).
5. N. M. W. Brunhuber, J. L. Mort, R. E. Christoffersen, N. O. Reich, *Biochemistry* **39**, 10730–10738 (2000).
6. M. C. Pirrung, *Acc. Chem. Res.* **32**, 711–718 (1999).
7. A. Bassan, T. Borowski, C. J. Schofield, P. E. M. Siegbahn, *Chem. Eur. J.* **12**, 8835–8846 (2006).
8. L. M. Mirica, J. P. Klinman, *Proc. Natl. Acad. Sci. U.S.A.* **105**, 1814–1819 (2008).
9. S. Shima *et al.*, *Science* **321**, 572–575 (2008).
10. J. M. Miller, E. E. Conn, *Plant Physiol.* **65**, 1199–1202 (1980).
11. D. R. Dilley *et al.*, *AoB Plants* **5**, plt031 (2013).
12. W.-K. Yip, S. F. Yang, *Plant Physiol.* **88**, 473–476 (1988).
13. J. M. Smith, R. N. Arteca, *Physiol. Plant.* **109**, 180–187 (2000).
14. D. Braga *et al.*, *Chem. Eur. J.* **8**, 1173–1180 (2002).
15. X. Zhang, U. Gross, K. Seppelt, *Angew. Chem. Int. Ed. Engl.* **34**, 1858–1860 (1995).
16. I. S. MacIntosh *et al.*, *Organometallics* **29**, 2063–2068 (2010).
17. U. Drück, W. Becker, G. Becker, *Z. Kristallogr.* **167**, 131–134 (1984).
18. F. H. Allen, *Acta Crystallogr. B* **58**, 380–388 (2002).
19. K. F. Purcell, *J. Am. Chem. Soc.* **91**, 3487–3497 (1969).
20. N. W. Alcock, G. Pennington, G. R. Willey, *Acta Crystallogr. C* **41**, 1549–1550 (1985).
21. E. E. Schweizer, C. J. Baldacchini, A. L. Rheingold, *Acta Crystallogr. C* **45**, 1236–1239 (1989).
22. M. Köckerling, J. B. Willems, *Z. Kristallogr., New Cryst. Struct.* **214**, 460 (1999).
23. A. Bernsdorf, M. Köckerling, *Z. Kristallogr., New Cryst. Struct.* **227**, 85–86 (2012).
24. I. Ling, Y. Alias, A. N. Sobolev, C. L. Raston, *Cryst. Eng. Comm.* **12**, 4321–4327 (2010).
25. K. Morokuma, *J. Chem. Phys.* **55**, 1236–1244 (1971).
26. K. Kitaura, K. Morokuma, *Int. J. Quantum Chem.* **10**, 325–340 (1976).
27. T. Ziegler, A. Rauk, *Theor. Chim. Acta* **46**, 1–10 (1977).
28. D. Himmel, I. Krossing, A. Schnepf, *Angew. Chem. Int. Ed.* **53**, 370–374 (2014).
29. I. V. Alabugin, B. Gold, M. Shatruk, K. Kovnir, *Science* **330**, 1047 (2010).
30. H. Zhou, W.-Z. Zhang, C.-H. Liu, J.-P. Qu, X.-B. Lu, *J. Org. Chem.* **73**, 8039–8044 (2008).
31. H. A. Duong, T. N. Tekavec, A. M. Arif, J. Louie, *Chem. Commun.* **2004**, 112–113 (2004).
32. J. D. Holbrey *et al.*, *Chem. Commun.* **2003**, 28–29 (2003).
33. N. Kuhn, M. Steimann, G. Weyers, *Z. Naturforsch. Teil B* **54**, 427–433 (1999).
34. A. M. Appel *et al.*, *Chem. Rev.* **113**, 6621–6658 (2013).
35. M. Shoukry, S. S. Hassan, *Cent. Eur. J. Chem.* **12**, 318–324 (2014).
36. J. J. Dwyer *et al.*, *Biophys. J.* **79**, 1610–1620 (2000).
37. B. E. García-Moreno *et al.*, *Biophys. Chem.* **64**, 211–224 (1997).
38. F. Mani, M. Peruzzini, P. Stoppioni, *Green Chem.* **8**, 995–1000 (2006).
39. F. A. Miller, C. H. Wilkins, *Anal. Chem.* **24**, 1253–1294 (1952).

The Gravity Field and Interior Structure of Enceladus

L. Iess,[1]* D. J. Stevenson,[2] M. Parisi,[1] D. Hemingway,[3] R. A. Jacobson,[4] J. I. Lunine,[5] F. Nimmo,[3] J. W. Armstrong,[4] S. W. Asmar,[4] M. Ducci,[1] P. Tortora[6]

The small and active Saturnian moon Enceladus is one of the primary targets of the Cassini mission. We determined the quadrupole gravity field of Enceladus and its hemispherical asymmetry using Doppler data from three spacecraft flybys. Our results indicate the presence of a negative mass anomaly in the south-polar region, largely compensated by a positive subsurface anomaly compatible with the presence of a regional subsurface sea at depths of 30 to 40 kilometers and extending up to south latitudes of about 50°. The estimated values for the largest quadrupole harmonic coefficients ($10^6 J_2 = 5435.2 \pm 34.9$, $10^6 C_{22} = 1549.8 \pm 15.6$, 1σ) and their ratio ($J_2/C_{22} = 3.51 \pm 0.05$) indicate that the body deviates mildly from hydrostatic equilibrium. The moment of inertia is around $0.335 MR^2$, where M is the mass and R is the radius, suggesting a differentiated body with a low-density core.

After Titan, Enceladus has been the most observed satellite by the Cassini spacecraft during its exploration of the Saturnian system. Images of this small moon (252 km radius) revealed a large plume ejected from the south-polar region, with the source being long fractures from which vapor and ice emerge as discrete jets (*1*). Concurrent observations of sodium and potassium salts in the plume (*2*), and the measured temperatures within the fractures (*3*),

strongly argue for the presence of liquid water in the subsurface source region. The plume exhibits a time variability well correlated to the predicted tidal stresses of the body (*4*).

The endogenic (nonsolar) power emitted from the south-polar region, derived from Cassini Composite Infrared Spectrometer data, is 15.8 GW, with a 20% formal uncertainty (*5*). This is equivalent to an average surface heat flux of ~20 mW/m^2 and is an order of magnitude larger than conventional estimates of tidal heating if Enceladus' current orbital eccentricity represents a so-called "equilibrium" resonant state with other satellites (*6*). It indicates time-variability in its internal properties (*7*), in a resonant state with other nearby moons (*8*), or in the rate of heat transport. In any or all of these cases, a plausible internal structure is that of a liquid water ocean overlain by a (thermally conductive) crust (*5*).

The design of the Cassini spacecraft does not allow radio tracking from Earth during remote-sensing observations. Therefore, only 3 of the 19 flybys of Enceladus completed so far have been used for gravity measurements. In these close encounters, the spacecraft was continuously tracked from ground antennas while flying within 100 km of the moon's surface, twice above the southern

[1]Dipartimento di Ingegneria Meccanica e Aerospaziale, Sapienza Università di Roma, via Eudossiana 18, 00184 Rome, Italy. [2]California Institute of Technology, 150-21 Pasadena, CA 91125, USA. [3]Department of Earth and Planetary Sciences, University of California Santa Cruz, 1156 High Street, Santa Cruz, CA 95064, USA. [4]Jet Propulsion Laboratory, California Institute of Technology, 4800 Oak Grove Drive, Pasadena, CA 91109, USA. [5]Department of Astronomy, Cornell University, Ithaca, NY 14850, USA. [6]Dipartimento di Ingegneria Industriale, Università di Bologna, I-47121 Forlì, Italy.

*Corresponding author. E-mail: luciano.iess@uniroma1.it

hemisphere (in the flybys labeled E9 and E19) and once over the northern hemisphere (E12) (9). We determined Enceladus' quadrupole gravity field and degree-3 zonal harmonic coefficient J_3 from measurements of spacecraft range-rate. With a radius ~10 times smaller than that of Titan, and about the same density, the gravitational signature of Enceladus in Doppler measurements is much weaker than that of Saturn's largest moon. However, the small perturbation due to J_3 (about 0.2 to 0.3 mm/s) is still clearly detectable by the Cassini tracking system, whose accuracy is 0.02 to 0.09 mm/s on a time scale of $\tau \approx 60$ s.

Microwave links between the onboard transponder and ground stations of NASA's Deep Space Network enabled precise measurements of the spacecraft range-rate. In addition to gravitational forces, our analysis accounts for the main nongravitational accelerations, most notably neutral particle drag exerted by the substantial gas plume formed by the jets of the south-polar region. Flying by the moon at latitudes below −70°, the spacecraft interacts with the plume at distances of up to 500 km from Enceladus' surface, although most of the effect is localized within 20 s from closest approach. Given the uncertainties in the gas density along the spacecraft flight path, and the short time scale of the interaction, the effect of the drag can be modeled as an unknown, impulsive, vectorial acceleration at closest approach at E9 and E19 (9). The orbital solutions yielded a velocity variation almost parallel to the spacecraft velocity, as expected for a drag force, of magnitude 0.25 mm/s for E9 and 0.26 mm/s for E19, which are comparable with the J_3 signature. The inclusion of the neutral particle drag in the south-polar flybys is therefore essential for obtaining Doppler residuals free of any signatures, which is essential for a faithful gravity solution.

As in previous Cassini gravity analyses (10, 11), the solution for Enceladus' gravity field (labeled as SOL1 in Table 1) was obtained from a multiple-arc analysis in which all data from the three flybys were fitted by using separate initial conditions for the spacecraft state vector at each arc (local parameters). The Enceladus state vector, the five degree-2 harmonic coefficients, and J_3 were considered global parameters common to all arcs. To

avoid biased estimates, the a priori uncertainties on the gravity coefficients were at least 30 times larger than were the formal uncertainties obtained from the orbital solution. The nongravitational accelerations due to anisotropic thermal emission from the three radioisotope thermoelectric generators and solar radiation pressure were modeled by using values determined by the spacecraft navigation team from the past 8 years of the Saturn tour. By processing the data into a multiple-arc least-squares filter, we were able to estimate local and global parameters (Table 1). Furthermore, the solution was proven to be stable with respect to perturbations of the dynamical model, such as the estimation of a full degree-3 field (9).

The ratio J_2/C_{22} differs from the value required for hydrostatic equilibrium ($J_2/C_{22} = 10/3$), suggesting that the satellite is not in a fully relaxed shape. The equipotential surface of the tidal, rotational, and gravitational potential (the latter limited to 2,0 and 2,2 harmonics) has semiaxis differences of $a\text{-}c = 6.00$ km and $b\text{-}c = 2.07$ km. The tesseral coefficients C_{21}, S_{21}, and S_{22} are null

within 3σ, indicating that the adopted rotational model (9) is correct and that the orientation of the principal axes is that expected for a tidally locked body with a fully damped pole. The estimated value of J_3 implies a 2.5 mGal, negative gravity anomaly at the south pole (Fig. 1).

The interpretation of Enceladus gravity presents a greater difficulty and uncertainty than usual, given the strikingly different appearances of the northern and southern hemisphere and the apparent confinement of endogenic activity to the high southern latitudes. Still, the deviation of J_2/C_{22} from 10/3 (the value for a laterally homogeneous body) is modest (of order 5%) and the non–degree-2 gravity is small (of order 2% relative to J_2), suggesting that there is some prospect of useful inferences.

The topography of Enceladus (12) is not that of a relaxed hydrostatic body under the action of tides and rotation in a synchronous orbit. Comparisons of the geoid heights with actual topography for the largest harmonics show differences of up to 1.2 km (Table 2).
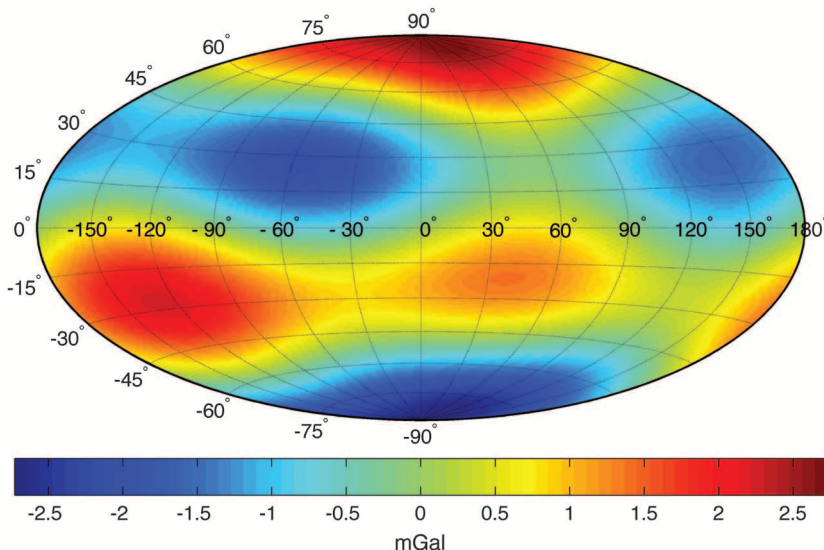

Fig. 1. Enceladus's gravity disturbances. The gravity field due to C21, S21, S22, and J3 (SOL1) is mapped onto the reference ellipsoid. The negative anomaly at the south pole, representing the asymmetry between the two hemispheres, is ~2.5 mGal.

Table 1. Solution for the gravity field of Enceladus. Estimated gravity harmonic coefficients from the multiarc fit of E9, E12, and E19 Doppler data.

Coefficient	SOL 1 Central value ± 1σ
J_2 (×10⁶)	5435.2 ± 34.9
C_{21} (×10⁶)	9.2 ± 11.6
S_{21} (×10⁶)	39.8 ± 22.4
C_{22} (×10⁶)	1549.8 ± 15.6
S_{22} (×10⁶)	22.6 ± 7.4
J_3 (×10⁶)	−115.3 ± 22.9
J_2/C_{22}	3.51 ± 0.05

Table 2. Comparison between Enceladus's geoid heights and actual topography. The existing differences for statistically nonzero harmonic coefficients result in contributions to Enceladus' gravity harmonics.

Harmonic	Topography* (km)	Equipotential height† (km)	Difference Δh (km)	Contribution of difference to gravity harmonics‡ (×10⁶)
−C_{20} (or J_2)	3.85 ± 0.02	2.680 ± 0.010	1.17 ± 0.03	1606 f_{20}
C_{22}	0.92 ± 0.02	0.780 ± 0.007	0.13 ± 0.03	183 f_{22}
−C_{30} (or J_3)	−0.38 ± 0.01	−0.030 ± 0.003	−0.35 ± 0.01	−349 f_{30}

*From (12), 2σ error bars.   †From Table 1, 2σ error bars (9).   ‡The geoid-to-topography ratio (GTR) for uncompensated topographic relief is $3\rho_c/(2l + 1)\,\overline{\rho}$ for degree l, where ρ_c is the crustal density (~0.93 g/cm³ is assumed) and $\overline{\rho}$ is the mean density (1.61 g/cm³), so GTR ($l = 2$) ≅ 0.35, and GTR ($l = 3$) ≅ 0.25. Here, f is the factor (different for each harmonics) by which the gravity due to the excess topography is compensated by a mass deficit or excess beneath the surface. For Airy compensation, $f = 1 − (1 − d/R)^l$, where d is depth of compensation, $R = 252$ km, and l is harmonic degree. The entries in the final column are given by Δh *GTR* f/(252km).

Either J_2 and C_{22} are fortuitously close to having ratio 10/3, or the nonhydrostatic contributions are small because of compensation (f is small). The degree-3 gravity, uncontaminated by tides and rotation, provides an estimate: $f_{30} \cong 115.3/349 \cong 0.33$, implying an Airy depth of compensation of ~32 km. This would in turn imply $f_{20} \cong 0.23$ (and f_{22} should equal f_{20} if compensation is isotropic); hence, the part of C_{22} arising from the topographic excess is $\sim 43 \times 10^{-6}$. Assuming that the hydrostatic contribution to this harmonic is then the remainder, 1507×10^{-6}, we infer that the most likely moment of inertia (MOI) of Enceladus is $0.336MR^2$, where M is the mass and R is the radius (9). If we choose the value of $f_{20} = f_{22}$ such that the hydrostatic part of J_2 is exactly 10/3 the hydrostatic part of C_{22}, we obtain $f \cong 0.27$, implying a depth of compensation of ~37 km and a moment of inertia of $\sim 0.335MR^2$.

If we instead use an iterative approach to self-consistently separate the hydrostatic and nonhydrostatic parts of both gravity and topography [(9), section S3.5], we obtain converging estimates of f_{20} and f_{22} (~0.25) when the moment of inertia is $0.335MR^2$, suggesting a compensation depth of ~34 km. The convergent $f_{20} = f_{22}$ is close to the value predicted on the basis of the observed f_{30}, confirming that the assumption of isotropic compensation is reasonable.

When we included elastic flexure as a means of supporting topography in our model, we found that in order to be consistent with the observed gravity-to-topography ratios, the elastic thickness must be less than 0.5 km, a value consistent with other estimates made from flexural analysis (13) and relaxation studies (14).

Results in this MOI range are compatible with a differentiated structure (15). For example, a value of $0.335MR^2$ can arise from a model with a relatively low core density of ~2.4 g/cm^3 and a H$_2$O mantle of density of 1 g/cm^3 and thickness of 60 km (9). The high heat flow and plume activity strongly suggests a differentiated structure, which is compatible with these results.

The data imply a great deal of compensation; if our assumption of Airy isostasy is correct, the inferred compensation depth of 30 to 40 km is most simply explained as the thickness of the ice shell overlying a liquid water layer. The large compensation excludes a very different kind of model, in which the main effect is the tidal and rotational response of a body with a nonradial symmetry of material properties. The tidal and rotational response of a body with a degree-1 variation in properties could introduce topography and gravity at degree 3, an example of mode coupling (16); but if this were responsible for the topographic distortion, then it would predict a much larger gravity distortion than is observed (yielding $f \sim 1$ instead of the observed much smaller values). For the same reason, a frozen-in tidal and rotational bulge from an earlier epoch (17) will not explain the observed gravity if that bulge has persisted in the ice mantle. A frozen-in deformation of the core (18) could in

principle explain the gravity, but the topography would still have to be highly compensated.

The presence of at least a regional south polar subcrustal sea suggests a model in which the mean temperature of the ice beneath the south pole is warmer than elsewhere, perhaps leading to a lower mean density of ~1% (corresponding to 100 K temperature excess and a coefficient of thermal expansion of $\sim 10^{-4}$ K^{-1}). But to satisfy the observed gravity, it is then necessary to insert a region of higher-density material roughly twice as large as that needed to offset the topographic depression alone and at a depth at least as great as the previous compensation depth estimates. If this material is water and is 8% denser than the surrounding ice, then a layer ~10 km thick is required, diminishing in thickness toward the lower southern latitudes. The total hydrostatic pressure at the base of this region would be in balance with the pressure at the same depth, plausibly at or near the base of the ice shell, in adjacent non–south polar regions that lack water, thus reducing the tendency for this layer to spread laterally. A highly concentrated mass anomaly at the south pole would predict $J_3 = -J_{2,\text{nh}}$. The data (Table 2) suggest $J_3 \sim -0.35 J_{2,\text{nh}}$, and this could be explained by a mass anomaly that extends from the pole to roughly 50° south latitude (9). However, the limitations of the data preclude high confidence in this inference.

Although the gravity data cannot rule out a global ocean, a regional sea is consistent with the gravity, topography, and high local heat fluxes (19) and does not suffer from the thermal problems that a global ocean encounters (19, 20). A global ocean would yield larger and potentially detectable longitudinal librations than are predicted for a solid body (21). The gravity coefficients and inferred MOI of Enceladus are not consistent with a forced 4:1 secondary libration (17, 22) at the 2σ level (9).

References and Notes

1. J. N. Spitale, C. C. Porco, *Nature* **449**, 695–697 (2007).
2. F. Postberg, J. Schmidt, J. Hillier, S. Kempf, R. Srama, *Nature* **474**, 620–622 (2011).
3. J. R. Spencer *et al.*, *Science* **311**, 1401–1405 (2006).
4. M. M. Hedman *et al.*, *Nature* **500**, 182–184 (2013).
5. C. J. A. Howett, J. R. Spencer, J. Pearl, M. Segura, *J. Geophys. Res.* **116**, (E3), E03003 (2011).
6. J. Meyer, J. Wisdom, *Icarus* **188**, 535–539 (2007).
7. G. W. Ojakangas, D. J. Stevenson, *Icarus* **66**, 341–358 (1986).
8. K. Zhang, F. Nimmo, *Icarus* **204**, 597–609 (2009).
9. Materials and methods are available as supplementary materials on *Science* Online.
10. L. Iess *et al.*, *Science* **327**, 1367–1369 (2010).
11. L. Iess *et al.*, *Science* **337**, 457–459 (2012).
12. F. Nimmo, B. G. Bills, P. C. Thomas, *J. Geophys. Res.* **116**, E11001 (2011).
13. B. Giese *et al.*, *Geophys. Res. Lett.* **35**, L24204 (2008).
14. M. T. Bland, K. N. Singer, W. B. McKinnon, P. M. Schenk, *Geophys. Res. Lett.* **39**, L17204 (2012).
15. G. Schubert, J. D. Anderson, B. J. Travis, J. Palguta, *Icarus* **188**, 345–355 (2007).
16. S. Zhong *et al.*, *J. Geophys. Res.* **39**, L15201 (2012).
17. C. C. Porco *et al.*, *Science* **311**, 1393–1401 (2006).
18. W. B. McKinnon, *J. Geophys. Res.* **118**, 1775 (2013).
19. G. Tobie, O. Cadek, C. Sotin, *Icarus* **196**, 642–652 (2008).
20. J. H. Roberts, F. Nimmo, *Icarus* **194**, 675–689 (2008).
21. N. Rambaux, J. C. Castillo-Rogez, J. G. Williams, Ö. Karatekin, *Geophys. Res. Lett.* **37**, L04202 (2010).
22. J. Wisdom, *Astron. J.* **128**, 484–491 (2004).

Geophysical and Geochemical Evidence for Deep Temperature Variations Beneath Mid-Ocean Ridges

Colleen A. Dalton,[1]*† Charles H. Langmuir,[2] Allison Gale[2,3]

The temperature and composition of Earth's mantle control fundamental planetary properties, including the vigor of mantle convection and the depths of the ocean basins. Seismic wave velocities, ocean ridge depths, and the composition of mid-ocean ridge basalts can all be used to determine variations in mantle temperature and composition, yet are typically considered in isolation. We show that correlations among these three data sets are consistent with 250°C variation extending to depths >400 kilometers and are inconsistent with variations in mantle composition at constant temperature. Anomalously hot ridge segments are located near hot spots, confirming a deep mantle-plume origin for hot spot volcanism. Chemical heterogeneity may contribute to scatter about the global trend. The coherent temperature signal provides a thermal calibration scale for interpreting seismic velocities located distant from ridges.

Mantle convection controls the evolution of the planet's interior and results in the motion of tectonic plates. The characteristics of this convection are governed by the density and viscosity of the mantle, which are functions of both temperature and composition.